

DUCTILE TEARING OF 2024 ALUMINUM ALLOY PANELS

F. BRON¹ & J. BESSON²

¹ Pechiney Centre de Recherches de Voreppe, BP 27, 38341 Voreppe Cedex, France

² Centre des Matériaux, ENSMP, CNRS UMR 7633, BP 87, Evry cedex 91003, France

ABSTRACT

Two 2024 aluminum alloys are studied. Their second phase volume fraction differ as well as their mean inter-particle spacing. Tests are carried out on large M(T) panels (used to determine the R-curve behavior) and smaller laboratory specimens. A finite element model taking into account ductile damage and plastic anisotropy is used to define transferability procedure between small and large samples as well as between both materials. The procedure is based on the definition of a material characteristic length proportional to the inter-particle spacing.

1 INTRODUCTION

AA2024 aluminum sheets are used to manufacture parts of the fuselage of aircrafts. Mechanical tests are performed on the sheets using large center-cracked tension panels M(T) in order to measure the crack initiation toughness as well as the R-curve behavior. With new improved materials, methods of analysis based on the linear fracture mechanics using plastic zone corrections can hardly be used since valid tests, according to the standard, would require very large panels (several meters) (ASTM [1]), (Chabanet [2]). Consequently, the prediction of the resistance to ductile tearing is of great interest in particular if the modeling is based on a good understanding of physical phenomena related to plastic deformation and ductile damage.

Two materials are investigated. They are two different grades of a 2024 aluminum alloy. One grade corresponds to the standard material. The second one corresponds to an improved grade in which the Fe and Si contents have been reduced. The main difference between the materials is their particle coarse content and particle spacing. The present study describes the application of a continuum damage model to simulate crack propagation. The plastic anisotropy is accounted for using a newly developed yield criterion (Bron [3]). The aim of the study is to develop a methodology allowing the simulation of the tests on wide M(T) plates for both materials based on a parameter adjustment on much smaller samples (KA specimens) carried out on one material only.

2 MATERIALS AND MECHANICAL TESTING

Two grades of 2024 aluminum alloy sheets (T4 heat-treated) with a nominal thickness of 1.6 mm were supplied by the aluminum manufacturer Pechiney. They are subsequently referred to as 2024-1 and 2024-2. Variant 2024-1 is a commercial alloy and variant 2024-2 is a high purity alloy improved for high damage tolerance. In the following, the rolling direction is referred to as L, the long transverse direction as T and the short transverse direction (thickness) as S. One of the major factors regarding damage tolerance is the presence of coarse intermetallic second phase particles and voids. They are nucleation sites for damage. The volume fraction of coarse intermetallic particles is largely influenced by the iron content which has been reduced in 2024-2 material. Most of those particles are composed of either Al-Cu-Fe-Mn(-Si) or Al-Cu-Mg. Second phase particles and voids have been characterized by image analysis on 2D micrographs. The materials also contain a small amount of preexisting cavities. Corresponding volume fractions are summarized on table 1.

	$f_p (10^{-3})$	$f_v (10^{-3})$	$\bar{d}_p (\mu\text{m})$
2024-1	13.0	1.2	19
2024-2	3.7	1.6	35

Table 1: Image analysis on 2024-1 and 2024-2 materials. f_p : particle volume fraction, f_v : void volume fraction, \bar{d}_p : particle mean spacing.

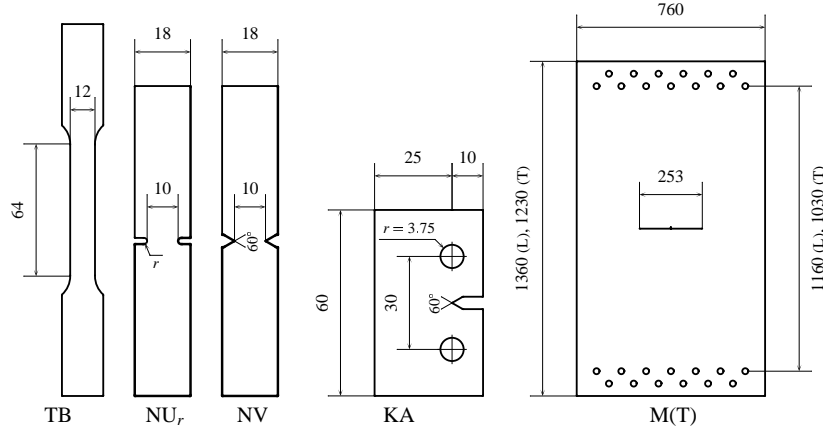


Figure 1: Specimens for mechanical tests (all dimensions in mm) – For TB specimen, longitudinal and transverse deformations are measured. For NU_r ($r = 0.5, 1$ or 2 mm) and NV, left and right opening displacements are measured; the mean value is used. For KA and M(T), the crack opening displacement and the crack length are measured. The notch radius of KA and NV is less than $60 \mu\text{m}$. The length of the M(T) specimen slightly differs in directions L and T because of the limited width of the as-received sheets.

Seven types of samples are used (Fig. 1). The TB sample is a conventional smooth tensile bar used to determine the elastic-plastic behavior. The differently notched samples $NU_{0.5}$, NU_1 , NU_2 and NV are used to characterize the behavior under various stress triaxiality ratios and to evaluate damage properties. Center-cracked tension panels M(T) are used to obtain a stable crack propagation over more than 60 mm at each side of the initial crack. This standard R-curve test (ASTM [1]) is expensive and could be replaced by tests on small sized Kahn specimens (KA) which also allow a stable crack propagation over more than 20 mm (ASTM [4]). The original crack length of large M(T) specimens is 253 mm after fatigue precracking. To prevent buckling two rigid face plates are affixed to the central portion of the specimen. KA specimens are not precracked. The radius of the V-notch is less than $60 \mu\text{m}$. For notched specimens, opening displacement is measured on both sides. TB and NU_r tests are used to adjust the model parameters describing the anisotropic plastic behavior (Bron [3]). KA specimens are used to adjust the model parameters describing ductile failure. Finally M(T) samples are used to check the validity of the model as they are simulated using the parameters obtained on small samples.

The fracture mechanisms were described by the authors in a previous publication (Bron [5]). The appearance of the macroscopic fracture surface depends on the notch severity. M(T), KA and NV exhibit the same aspect: the crack initiates with a flat triangular shape perpendicular to the loading direction (Fig. 2). The remaining fracture surface is slanted with a 45° angle with respect to the loading direction. When notch severity decreases ($NU_{0.5}$) the triangle diminishes in size and finally,

for NU₁, NU₂ and smooth specimens, there is no triangle at all and the whole surface is slanted. Voids are first initiated at intermetallic particles in both cases. In the flat triangular region, large voids grow from the particles up to coalescence by “internal necking” (Thomason [6]). In slanted regions, coalescence occurs by a “void sheet mechanism” (Garrison [7]) which is associated with the creation of smaller dimples in the inter-void ligaments.

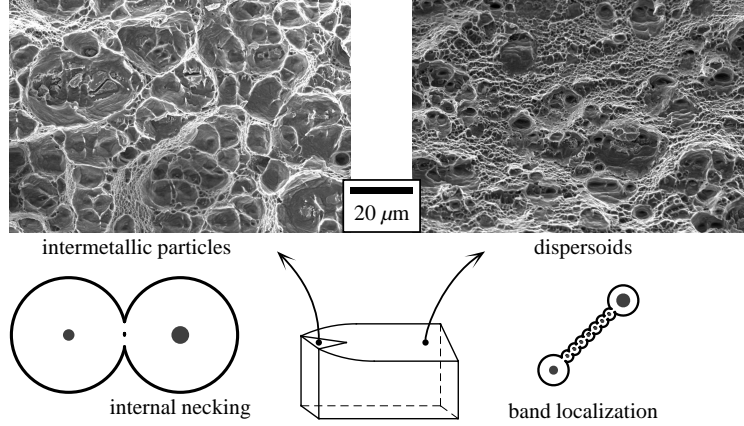


Figure 2: Two failure mechanisms: internal necking (left) or localization of the deformation (right).

3 MODELING

The constitutive model for porous materials proposed in (Rousselier [8]) and extended in (Tanguy [9]) is used. Damage is represented by a single scalar variable, the porosity f . The plastic flow potential, ϕ , is written as:

$$\phi = \sigma_* - R(p) \quad (1)$$

where $R(p)$ represents the hardening behavior of the undamaged material. p is a scalar measure of the plastic strain. The effective stress, σ_* , is defined by:

$$\psi = \frac{\sigma_a}{(1-f)\sigma_*} + \frac{2}{3}fD \exp\left(\frac{3q}{2} \frac{\sigma_m}{(1-f)\sigma_*}\right) - 1 \stackrel{\text{def.}}{=} \sigma_* \quad (2)$$

where σ_a is an equivalent stress and σ_m the mean stress D and q are material parameters adjusted from experiments. σ_a does not correspond to the usual von Mises stress but is defined according to (Bron [3]) in order to account for plastic anisotropy. The plastic flow is obtained assuming normality so that the plastic strain rate tensor is given by:

$$\dot{\underline{\epsilon}}_p = (1-f)\dot{p} \frac{\partial \phi}{\partial \underline{\sigma}} = (1-f)\dot{p} \frac{\partial \sigma_*}{\partial \underline{\sigma}} \quad (3)$$

where $\underline{\sigma}$ is the stress tensor. Noting that σ_* is an homogeneous function of degree 1 of $\underline{\sigma}$ Euler's theorem applies so that:

$$\underline{\sigma} : \dot{\underline{\epsilon}}_p = (1-f)\sigma_*\dot{p} \quad (4)$$

This relation is interpreted as the equality between the macroscopic plastic work (left hand-side) and the microscopic plastic work (right hand-side). The evolution of the porosity f is given by mass conservation modified to account for strain controlled void nucleation (Chu [10]):

$$\dot{f} = (1 - f)\text{trace}\dot{\underline{\underline{\epsilon}}}_p + A_n \dot{p} = \left((1 - f)^2 \frac{\partial \sigma_*}{\partial \underline{\underline{\sigma}}} : \underline{\underline{1}} + A_n \right) \dot{p}. \quad (5)$$

Nucleation correspond to cracking/debonding of second phase particles.

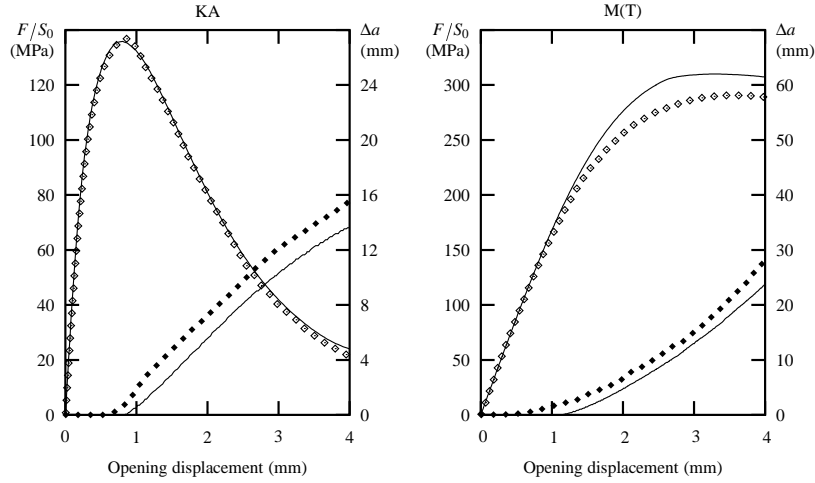


Figure 3: Simulations (lines) on KA and M(T) samples for material 2024-2 compared to experiments (symbols); loading is in the T direction. Empty symbols are used for the load F/S_0 and black symbols for the crack advance Δa .

4 FINITE ELEMENT SIMULATION

Calculations were done using quadratic elements with reduced integration. The region where the crack propagates was meshed with 20 node 3D elements (8 integration points) and far from this region, plane stress elements are used. Besides, due to the symmetries, only an eighth of the samples is meshed (a fourth for KA samples). A post-increment procedure removes broken elements. In the case of 3D bricks with twenty nodes and eight Gauss points, it is performed when four Gauss points are broken. Details on the simulations procedures can be found in (Besson [11])

When modeling crack propagation using continuum damage mechanics, the crack is a thin volume which height is half the element height in the case of quadratic elements. Thus crack growth is very much affected by the height of the elements ℓ in the crack region which should be considered as a material parameter (Rivalin [12]), (Xia [13]), (Skallerud [14]). The two other mesh dimensions only influence the accuracy of the results as a classical mesh refinement. Indeed the crack growth is also controlled by the damage parameters D and q . The mesh size only affects the behavior in the crack region but the damage parameters modify the behavior in the whole sample. Thus an optimal mesh size should allow the use of the same set of damage parameters for all stress/strain conditions.

Previous publications show that the order of magnitude of the mesh size should be the inter-particle spacing (Rousselier [8]), (Brocks [15]), (Steglich [16]), (Gullerud [17]). The mean second phase particle spacing \bar{d} is estimated from the surface particle density (table. 1). In the present case, \bar{d} is so small that a mesh corresponding to this size would be too large to allow to run the simulations.

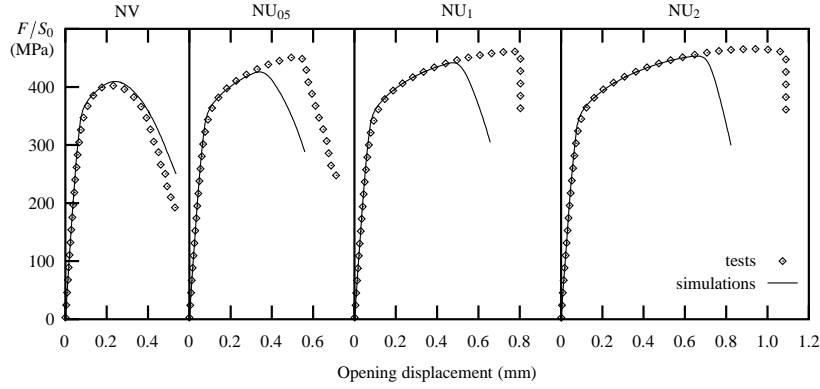


Figure 4: Simulations on notched samples for material 2024-2; loading is in the T direction.

In this work the mesh dimension, ℓ , was fixed *a priori* for material 2024-2: $\ell_{2024-2} = 175\mu\text{m}$. The mesh size for the second grade (2024-1) is defined so that: $\ell_{2024-2}/\ell_{2024-1} = \bar{d}_{2024-2}/\bar{d}_{2024-1}$ so that the mesh size is scaled according to the microstructural characteristic length. The initial porosity is taken from the image analysis as well as the particle volume fraction which can nucleate new cavities. Based on observations which indicate that all particles are broken in a tensile test at the onset of necking the nucleation rate is given by: $A_n = (f_p/p_0)$ if $p < p_0$ and $A_n = 0$ otherwise. p_0 is the plastic strain at the onset of necking ($p_0 = 0.16$ for both materials). The damage parameters, $D = 4.6$ and $q = 1.0$, were adjusted to fit results on KA samples for material 2024-2 only. Material 2024-1 is simulated using the same values for D and q and values for the initial porosity and the nucleation rate corresponding to image analysis results. The adjustment of the parameters used to represent plastic anisotropy is described in (Bron [3]).

5 RESULTS AND CONCLUSIONS

The present simulation cannot reproduce slant fracture and crack advance remains flat throughout the calculation. It should however be outlined that, in the literature, the flat to slant crack path change has not yet been satisfactorily simulated. It is believed that a very fine mesh (mesh size of about the inter-particle distance) is required to perform the calculation of the flat to slant transition. Such calculations require a computational power that is not yet available. The present calculation is able to represent both the crack growth rate and the load level.

Fig. 3 compares the experimental and simulated load vs. opening and crack advance (Δa) vs. opening curves for both KA and M(T) specimens for material 2024-2. The crack length is slightly underestimated. This is possibly due to the inability of the model to capture the transition between flat and slanted fracture. In the case of the M(T) specimen the load is overestimated; this is due to the partial buckling of the large plate during testing which is not fully prevented using an anti-buckling setup during the test (Roychowdhury [18]).

Fig. 4 compares experimental and simulated loads for NV and NU_r specimens. A good agreement is obtained for the deeply notched specimen (NV). For other specimens the ductility is underestimated. This discrepancy is related to the fact that the mesh size was fixed to be able run calculations and not adjusted to be representative of the material rupture characteristic length. This leads to a high value of the adjusted D which is suitable to simulate crack propagation with the chosen mesh size but leads to early rupture in notched specimens.

Fig. 5 compares the experimental and simulated load vs. opening and crack advance curves for

material 2024-1. A good agreement is obtained considering that the damage parameters D and q were not fitted. This also shows that considering that the interparticle mean distance is the rupture characteristic length is consistent. A better agreement could have been obtained considering the mean distance between particles and voids considered as a single defect population as in that case the $\bar{d}_{2024-1}/\bar{d}_{2024-2}$ would have been slightly larger.

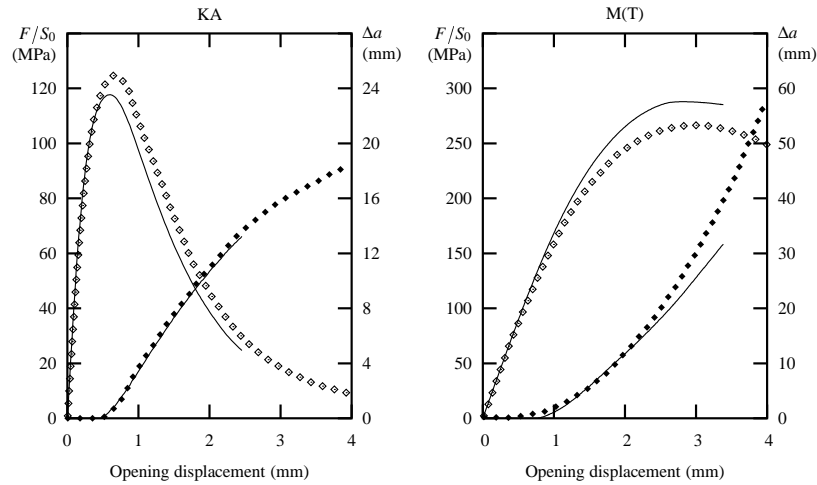


Figure 5: Simulations on KA and M(T) samples for material 2024-1; loading is in the T direction. Empty symbols are used for the load F/S_0 and black symbols for the crack advance Δa .

REFERENCES

- 1 ASTM (1999) *Annual Book of ASTM Standards*, **03.01**, 509–521.
- 2 Chabanet, O., Steglich, D., Besson, J., Heitmann, V., Hellmann, D. and Brocks, W. (2003) *Comput. Mater. Sci.*, **26**, 1–12.
- 3 Bron, F. and Besson, J. (2004) *Int. J. Plasticity*, **20** (4–5), 937–963.
- 4 ASTM (2001) *Annual Book of ASTM Standards*, **02.02**.
- 5 Bron, F., Besson, J. and Pineau, A. (accepted) *Mater. Sci. Engng A*.
- 6 Thomason, P. F. (1985) *Acta Metall.*, **33** (6), 1079–1085.
- 7 Garrison, W. M. and Moody, N. R. (1987) *J. Phys. Chem. Solids*, **48** (11), 1035–1074.
- 8 Rousselier, G. (1987) *Nuclear Engng Design*, **105**, 97–111.
- 9 Tanguy, B. and Besson, J. (2002) *Int. J. Fract.*, **116** (1), 81–101.
- 10 Chu, C. C. and Needleman, A. (1980) *J. Engng Mater. Tech.*, **102** (3), 249–256.
- 11 Besson, J., Steglich, D. and Brocks, W. (2001) *Int. J. Solids Struct.*, **38** (46–47), 8259–8284.
- 12 Rivalin, F., Besson, J., Di Fant, M. and Pineau, A. (2001) *Engng Fract. Mech.*, **68**, 347–364.
- 13 Xia, L., Shih, C. F. and Hutchinson, J. W. (1995) *J. Mech. Phys. Solids*, **43** (3), 389–413.
- 14 Skallerud, B. and Zhang, Z. L. (1999). In: *Fatigue and fracture mechanics: 29th vol. ASTM STP 1332*, Panontin, T. L. and Sheppard, S. D. (Eds.), pp. 201–214.
- 15 Brocks, W., Hao, S. and Steglich, D. (1996) *J. Phys. IV*, **6** (6), 43–52.
- 16 Steglich, D. and Brocks, W. (1998) *Fatigue Fract. Engng Mater. Struct.*, **21** (10), 1175–1188.
- 17 Gullerud, A., Gao, X., Dodds Jr, R. and Haj-Ali, R. (2000) *Engng Fract. Mech.*, **66** (1), 65–92.
- 18 Roychowdhury, S., Roy, Y. and Dodds Jr, R. (2002) *Engng Fract. Mech.*, **69** (8), 983–1002.